Search for Supersymmetry in Diphoton Events with Large Missing Transverse Momentum in 8 TeV pp Collision Data with the ATLAS Detector

The ATLAS Collaboration

Abstract

A search for diphoton events with large missing transverse momentum has been performed using $20.3\,\mathrm{fb}^{-1}$ of proton–proton collision data at a centre-of-mass energy of 8 TeV recorded with the ATLAS detector. No excess of events was observed above the Standard Model prediction and both model-independent and model-dependent 95% confidence level exclusion limits are set. Using a selection optimized to detect evidence for a generalised model of gauge-mediated supersymmetry breaking with a bino-like lightest neutralino $\tilde{\chi}_1^0$, gluinos below 1280 GeV and degenerate triplets of wino-like charginos and next-to-lightest neutralinos below 570 GeV are excluded for any $\tilde{\chi}_1^0$ mass above 50 GeV.

1 Introduction

Supersymmetry (SUSY) [1–9] introduces a symmetry between fermions and bosons, resulting in a SUSY partner (sparticle) with identical Standard Model (SM) quantum numbers except a difference of half a unit of spin for each SM particle. As none of these sparticles have been observed, SUSY must be a broken symmetry if realised in nature. Assuming R-parity conservation [10–14], sparticles have to be produced in pairs. These would then decay through cascades involving other sparticles until the lightest SUSY particle (LSP) is produced, which is stable.

In gauge-mediated SUSY breaking (GMSB) models [15–20] the LSP is the gravitino $\tilde{G}$. GMSB experimental signatures are largely determined by the nature of the next-to-lightest SUSY particle (NLSP). In this study the NLSP was assumed to be the SUSY partner of the SM U(1) gauge boson, i.e., a bino-like lightest neutralino $\tilde{\chi}_1^0$. Since the bino has a photonic branching fraction of at least $\cos^2 \theta_W$ the final decay in the cascade is predominantly $\tilde{\chi}_1^0 \rightarrow \gamma \tilde{G}$. Two neutralinos are produced in each event, leading to final states with $\gamma\gamma + E_T^{\text{miss}}$, where E_T^{miss} is the missing transverse momentum that arises from the undetected gravitinos and neutrinos.

Two different instances of a generalised GMSB SUSY model, referred to as models of 'General Gauge Mediation' (GGM) [21, 22], were considered in this study. For the first instance ('gluino-bino' or 'strong-production'), the next-to-next-to-lightest supersymmetric particle (NNLSP) was assumed to be an octet of gluino ($\tilde{g}$) states, with all other SUSY partners at inaccessibly high mass, resulting in SUSY events induced by gluino-pair production. Note that, due to its possession of the SM couplings of the U(1) gauge boson, direct production of the bino-like NLSP, either in pairs or in association with an NNLSP, is highly suppressed. These gluinos were assumed to decay through short cascades involving SM partons to the bino-like neutralino NLSP, as depicted in the left-hand diagram of Fig. 1. This leads to events with two final state photons, significant E_T^{miss}, and a large amount of visible transverse energy. For the second instance ('wino-bino' or 'electroweak-production'), the NNLSP was assumed to be a nearly-degenerate triplet of partners of the SM SU(2) gauge bosons, known collectively as the wino ($\tilde{W}$) and denoted by $\tilde{\chi}_2^0$ and $\tilde{\chi}_1^\pm$, resulting in SUSY events induced by wino pair production ($\tilde{\chi}_2^0 \tilde{\chi}_1^\pm$; $\tilde{\chi}_1^+ \tilde{\chi}_1^-$). The winos were again assumed to decay via short cascades involving SM bosons and fermions to the NLSP bino, leading to events with two final state photons, significant E_T^{miss}, but only a moderate amount of visible transverse energy. A typical wino-bino GGM-model production and decay process is depicted in the right-hand diagram of Fig. 1; if the mass difference between the produced wino and decay-product bino is smaller than that of the corresponding electroweak boson, the wino decay produces SM fermions directly. Jets may be produced in the cascades directly from the gluino decays, or from the decays of SM vector bosons that are formed as intermediate states in the decay chain.

For both instances, the mass of the bino-like NLSP was treated as a free parameter, and varied between $50\,\text{GeV}$ and the mass of the NNLSP. The NNLSP mass was itself taken as a free parameter, with no explicit limit imposed upon its range. All other SUSY partner masses were decoupled; i.e., set to inaccessibly large values. Further model parameters are fixed to $\tan\beta = 1.5$ and $c\tau_{\text{NLSP}} < 0.1\,\text{mm}$, where $\tan\beta$ is the ratio of vacuum expectation values of the two SUSY Higgs doublets. The GGM production and decay properties are insensitive to the value of $\tan\beta$ and so the choice of the value 1.5 is arbitrary; the imposition of the upper limit on $c\tau_{\text{NLSP}}$ ensures that the bino decay is prompt. All signal models also include a fundamental scalar of mass $126\,\text{GeV}$ that has SM-like Higgs-boson couplings.

This note reports on a search for diphoton ($\gamma\gamma$) events with large E_T^{miss} in $20.3\,\text{fb}^{-1}$ of proton–proton (pp) collision data at a centre-of-mass energy $\sqrt{s} = 8\,\text{TeV}$ recorded with the ATLAS detector at the Large Hadron Collider (LHC) in 2012, interpreted in terms of the two GGM scenarios described above. This result extends a prior ATLAS study performed at $\sqrt{s} = 7\,\text{TeV}$ with $4.8\,\text{fb}^{-1}$ [23] that searched for evidence for the gluino-bino model, setting a lower limit of $1070\,\text{GeV}$ on the gluino mass for any value of bino mass [23]. No prior search has been performed for evidence of the wino-bino model.
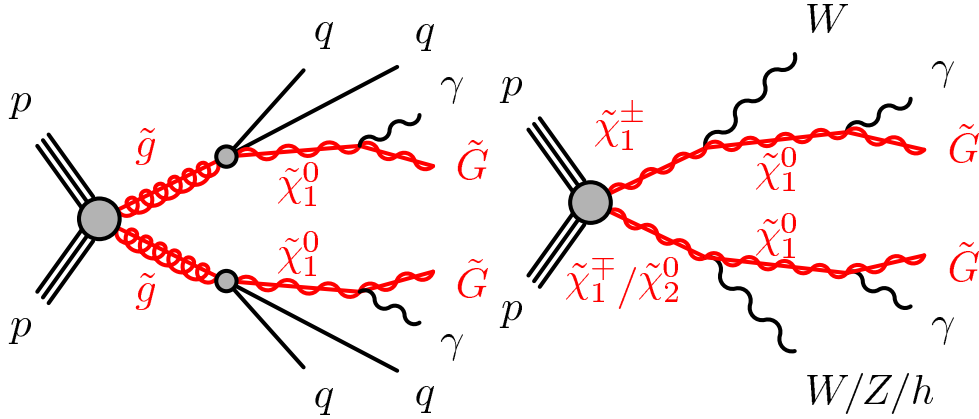
Figure 1: Typical production and decay-chain processes for the strong-production (left) and electroweak-production (right) instances of the GGM model.

2 Simulated samples

For the GGM models under study, the SUSY mass spectra were calculated using SUSPECT 2.41 [24] and SDECAY 1.3 [25]. The Monte Carlo (MC) SUSY signal samples were produced using HERWIG++ 2.5.1 [26] with MRST2007 LO* [27] parton distribution functions (PDF). Signal cross-sections were calculated to next-to-leading order (NLO) in the strong coupling constant, including, for the case of strong production, the resummation of soft gluon emission at next-to-leading-logarithmic accuracy (NLO+NLL) [28–32]. Diagrams resulting in squark production, or involving one or more squark propagators, were not considered. The nominal cross-section and the uncertainty were taken from an envelope of cross-section predictions using different PDF sets and factorisation and renormalisation scales, as described in Ref. [33]. The strong-production GGM signal was simulated over an area of the GGM parameter space that ranges from 1100 GeV to 1500 GeV for the gluino mass, while the neutralino mass ranges between 50 GeV and the gluino mass. The electroweak-production GGM signal was simulated over a region of the GGM parameter space that ranges from 500 GeV to 800 GeV for the wino mass, with the neutralino mass ranging between 50 GeV and the wino mass.

While most of the backgrounds to the two GGM models under examination were estimated through the use of control samples selected from data (to be described below), optimization studies and studies guiding the development of the control samples made use of the following MC samples. The simulation of gauge-boson production included events with up to five accompanying partons. Gauge boson production without an additional prompt photon was simulated with the ALPGEN [34] Monte Carlo generator (version 2.14) interfaced to HERWIG version 6.5.2 for showering and fragmentation processes, and to JIMMY [35] for simulation of the underlying event. Parton distributions were provided by the CTEQ6L1 [36] functions. W-boson-plus-photon production was also simulated via ALPGEN interfaced to HERWIG and JIMMY, but made use of the CT10 [37] parton distribution functions. The $Z\gamma$ process was simulated using SHERPA 1.4.1 [38], again making use of the CT10 parton distribution functions. The $t\bar{t}$ process was simulated with the MC@NLO [39, 40] generator, including full next-to-leading order QCD corrections, and making use of the CT10 parton densities. Parton showering and fragmentation was again simulated with the HERWIG event generator with JIMMY generating the underlying event.

The photon+jet(s) process was simulated in a similar manner to the $W^{\pm}$ or Z samples using ALPGEN interfaced to HERWIG and JIMMY and the CTEQ6L1 parton distribution function. A generator-level requirement of $p_T^{\gamma} > 35$ GeV was applied. Additional photon+jet(s) samples were used, simulated with SHERPA and making use of the CT10 parton distribution functions, with $p_T^{\gamma} > 45$ GeV, $p_T^{\gamma} > 70$ GeV

2

and $p_T^\gamma > 95\,\text{GeV}$. The prompt diphoton sample was generated with PYTHIA [41] version 6.4.23, and included the subprocesses $gg \to \gamma\gamma$ and $q\bar{q} \to \gamma\gamma$, with the requirement that there be at least two prompt photons with generator-level transverse momentum greater than 20 GeV. Parton densities were modeled according to the MRST 2007 LO* [27] functions.

The background from $Z(\to \nu\bar{\nu}) + \gamma\gamma$ production – the only background estimated directly from MC – was simulated using the SHERPA MC generator, normalized to a cross-section calculated at LO using MadGraph 5 [42] with the CTEQ6L1 PDF, and then corrected by a K-factor of 2.0 ± 1.0 [43]. The background from $W(\to \ell\nu) + \gamma\gamma$ production was simulated using the Alpgen MC generator, although the overall normalization was set via a study making use of data events containing two photons and a charged lepton (to be discussed below).

All MC samples were processed through the GEANT4-based simulation [44] of the ATLAS detector [45], or, where appropriate, a simulation of the ATLAS detector based on parametrized calorimeter shower shapes in the calorimeter, and GEANT4 elsewhere. The variation of the number of pp interactions per bunch crossing ('pileup') as a function of the instantaneous luminosity was taken into account by overlaying simulated minimum bias events according to the observed distribution of the number of pileup interactions in data, with an average of 21 interactions per event.

3   ATLAS detector

The ATLAS detector [46] is a multi-purpose apparatus with a forward-backward symmetric cylindrical geometry and nearly 4π solid angle coverage[1]. Closest to the beamline are tracking devices comprised of layers of silicon-based pixel and strip detectors covering $|\eta| < 2.5$ and straw-tube detectors covering $|\eta| < 2.0$, located inside a thin superconducting solenoid that provides a $2\,\text{T}$ magnetic field. Outside the solenoid, fine-granularity lead/liquid-argon electromagnetic (EM) calorimeters provide coverage for $|\eta| < 3.2$ to measure the energy and position of electrons and photons. A presampler, covering $|\eta| < 1.8$, is used to correct for energy lost upstream of the EM calorimeter. A steel/scintillating-tile hadronic calorimeter covers the region $|\eta| < 1.7$, while copper and liquid-argon technology is used for hadronic calorimeters in the end-cap region $1.5 < |\eta| < 3.2$. In the forward region $3.2 < |\eta| < 4.9$ liquid-argon calorimeters with copper and tungsten absorbers measure the electromagnetic and hadronic energy. A muon spectrometer, used to identify and measure the momentum of muons, surrounds the calorimeter and consists of three superconducting toroidal magnet systems each comprised of eight toroidal coils, tracking chambers, and detectors for triggering.

4   Reconstruction of physics objects and observables

The reconstruction of converted and unconverted photons and of electrons is described in Refs. [47] and [48], respectively. Both electrons and photons were identified via calorimeter shower shapes and the presence or absence of an associated charged track. Electron candidates were required to have $E_T > 25$ GeV. Photon candidates were required to have $E_T > 50$ GeV, to be within $|\eta| < 2.37$, and to be outside the transition region $1.37 < |\eta| < 1.52$ between the barrel and the end-cap calorimeters. The analysis made use of both 'loose' and 'tight' photons [47], identified on the basis of the characteristics of the longitudinal and transverse shower development in the EM calorimeter. Photon candidates were removed if they were found to coincide with an identified electron. Finally, an 'isolation' requirement was imposed, whereby photon candidates were removed if more than $4\,\text{GeV}$ of transverse energy was

---

[1]ATLAS uses a right-handed coordinate system with its origin at the nominal interaction point (IP) in the centre of the detector and the z-axis along the beam pipe. The x-axis points from the IP to the centre of the LHC ring, and the y-axis points upward. Cylindrical coordinates (R, ϕ) are used in the transverse plane, ϕ being the azimuthal angle around the beam pipe. The pseudorapidity is defined in terms of the polar angle θ as $\eta = -\ln\tan(\theta/2)$, and the transverse energy E_T as $E_T = E\sin\theta$.

observed in a cone of $\Delta R \equiv \sqrt{\Delta\eta^2 + \Delta\phi^2} < 0.4$ surrounding the photon's deposition in the calorimeter, after correcting for contributions from pileup and the deposition ascribed to the photon itself.

Jets were reconstructed using the anti-k_t jet algorithm [49] with four-momentum recombination and radius parameter $R = 0.4$, and were required to have $p_{\mathrm{T}} > 30\,\mathrm{GeV}$ and $|\eta| < 2.8$.

The value of $E_{\mathrm{T}}^{\mathrm{miss}}$ was calculated from energy deposits in the calorimeter with $|\eta| < 4.9$, and from reconstructed muons. The energy deposits were associated with reconstructed objects (jets, photons, electrons) and calibrated accordingly. Energy deposits not associated with a reconstructed object were calibrated according to their energy sharing between the EM and hadronic calorimeters.

From these reconstructed objects, a number of observables were formed that help discriminate between GGM signal and SM backgrounds. The photon-$E_{\mathrm{T}}^{\mathrm{miss}}$ separation $\Delta\phi_\gamma^{\mathrm{min}}$ was defined as the minimum azimuthal angle between the $E_{\mathrm{T}}^{\mathrm{miss}}$ direction and either of the two selected photons. The jet-$E_{\mathrm{T}}^{\mathrm{miss}}$ separation $\Delta\phi_{\mathrm{jet}}^{\mathrm{min}}$ was defined as the minimum azimuthal angle between the $E_{\mathrm{T}}^{\mathrm{miss}}$ direction and the two highest-p_{T} reconstructed jets, where reconstructed jets were required to have $p_{\mathrm{T}} > 75$ GeV; it was found that using a lower value of p_{T} for the construction of $\Delta\phi_{\mathrm{jet}}^{\mathrm{min}}$ reduced the effectiveness of selection requirements based upon it. If there was no such reconstructed jet, the value of $\Delta\phi_{\mathrm{jet}}^{\mathrm{min}}$ was set to a large default value.

The total visible transverse energy H_{T} was calculated as the sum of the magnitude of the transverse energy of the two selected photons and any additional leptons and jets in the event, where jets were required to have $p_{\mathrm{T}} > 30$ GeV. The total effective mass M_{eff} was defined as the sum of H_{T} plus the magnitude $E_{\mathrm{T}}^{\mathrm{miss}}$ of the missing transverse energy vector.

5 Data analysis

The data sample, corresponding to an integrated luminosity of $20.3 \pm 0.7\,\mathrm{fb}^{-1}$ [50], was selected by a trigger requiring two loose photon candidates with $E_{\mathrm{T}} > 40\,\mathrm{GeV}$. Vertex candidates for the pp interaction point were identified using reconstructed tracks. The primary vertex, corresponding to the hard scattering interaction, was chosen to be the vertex candidate with the largest sum of p_{T}^2 of the associated tracks. To ensure that activity recorded in the event resulted from a beam collision, events were required to have at least one vertex with more than four associated tracks. A series of requirements based on deposition patterns in the hadronic and EM calorimeter were applied to discriminate against energy deposits arising from calorimeter noise, beam halo and cosmic rays; if any jet was classified as such, the event was rejected. Events were also rejected if a muon was detected whose trajectory was not consistent with having arisen from the primary vertex or the decay of a particle containing a heavy quark. Events were then required to contain at least two tight photon candidates with $E_{\mathrm{T}} > 75\,\mathrm{GeV}$, which MC studies suggested would provide the greatest separation between signal and SM background for a broad range of the parameter space of the new physics scenarios under consideration in this search. In order to have the search remain as model-independent as possible, no requirement was placed on the number of jets or leptons present in the events.

A total of 17458 isolated $\gamma\gamma$ candidate events passing these selection requirements were observed in the data sample. The E_{T} distribution of the leading and sub-leading photon for events in this sample are shown in Fig. 2. Also shown are the E_{T} spectra expected for two characteristic signal model points: $m_{\tilde{g}} = 1300\,\mathrm{GeV}$ and $m_{\tilde{\chi}_1^0} = 1050\,\mathrm{GeV}$ (gluino production), and $m_{\tilde{W}} = 600\,\mathrm{GeV}$ and $m_{\tilde{\chi}_1^0} = 500\,\mathrm{GeV}$ (wino production). Figure 3 shows the M_{eff} distribution of selected diphoton events, with those of the same signal models overlaid. At this stage of the selection, prior to the application of requirements that eliminate events with poorly reconstructed $E_{\mathrm{T}}^{\mathrm{miss}}$, background estimates are not reliable. Thus, no background levels are shown for either Fig. 2 or 3.

GGM SUSY events will potentially be mimicked by SM events from QCD processes with prompt photons and large $E_{\mathrm{T}}^{\mathrm{miss}}$ arising from the occasional poor reconstruction of particles and jets, or from weak
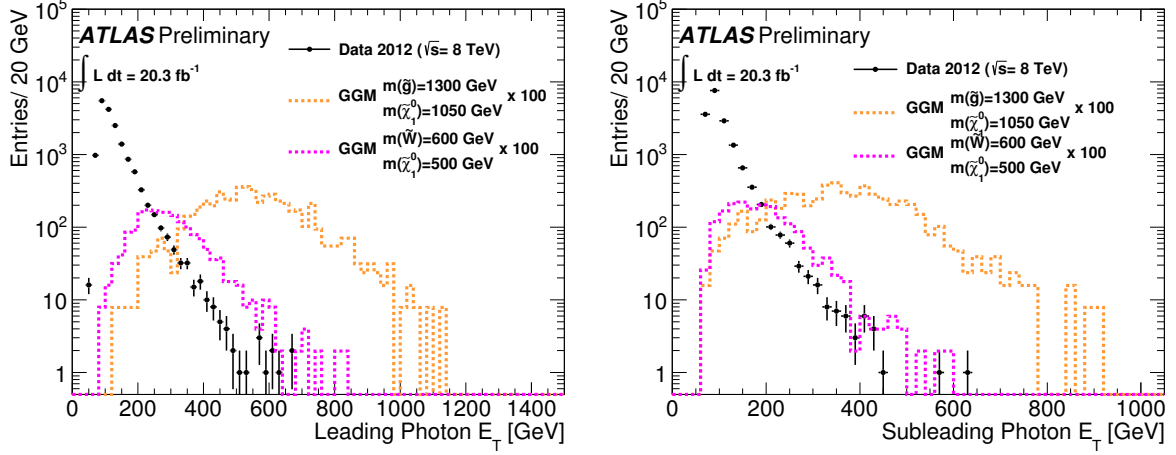
Figure 2: The E_T spectrum of the leading photon (left) and subleading (right) photon in the $\gamma\gamma$ candidate events in the data (points, statistical uncertainty only) together with the leading-photon E_T spectra obtained from gluino production GGM MC samples for $m_{\tilde{g}} = 1300\,\text{GeV}$ and $m_{\tilde{\chi}_1^0} = 1050\,\text{GeV}$, and wino production GGM MC for $m_{\tilde{W}} = 600\,\text{GeV}$ and $m_{\tilde{\chi}_1^0} = 500\,\text{GeV}$. The signal samples are multiplied by a factor of 100 for visibility.

decays of energetic mesons. Backgrounds will also arise from W and Z boson production accompanied by one or more prompt photons, with E_T^{miss} due to neutrinos arising from gauge boson decays. To maximise the sensitivity of this analysis over a wide range of model parameters that may lead to different kinematic properties, four different signal regions (SRs) were defined based on the reconstructed values of E_T^{miss}, H_T, M_{eff}, $\Delta\phi_{\gamma}^{\text{min}}$ and $\Delta\phi_{\text{jet}}^{\text{min}}$. Two of these (SP1, SP2) were geared towards the observation of strongly-produced SUSY states at high mass, while the other two (WP1, WP2) were geared towards the observation of weakly-produced SUSY states at intermediate mass. In addition, a fifth, 'model-independent' signal region (MIS) was defined based only on the observed behavior of the SM background estimate, imposing no requirement on the mass scale variables H_T or M_{eff}, and choosing a minimum value of E_T^{miss} that suppressed the level of QCD-induced backgrounds to that arising from electroweak sources. For the search for wino production, and for the MIS selection, for which observable mass scales may be relatively low, the M_{eff} observable was found to be heavily correlated with E_T^{miss}, and thus H_T, rather than M_{eff}, was used for the penultimate selection requirement. The opposite choice was made for the gluino production search.

Selection SP1 was geared towards GGM model points initiated by gluino production with a subsequent decay to a high-mass bino, leading to a selection featuring both a high E_T^{miss} requirement as well as a high M_{eff} requirement. Selection SP2 was geared towards GGM model points featuring gluino production with a subsequent decay to a low-mass bino, leading to a selection featuring an intermediate E_T^{miss} requirement and a high M_{eff} requirement. Selection WP1 was geared towards GGM model points featuring wino production with a subsequent decay to a high-mass bino, leading to a selection featuring a high E_T^{miss} requirement but only a moderate H_T requirement. Selection WP2 was geared towards GGM model points featuring wino production with a subsequent decay to a low-mass bino, leading to a selection featuring moderate requirements on both E_T^{miss} and H_T. For all five selections, the requirement $\Delta\phi_{\text{jet}}^{\text{min}} > 0.5$ was found to be a good discriminant for rejecting events with poorly-reconstructed E_T^{miss}. A requirement of $\Delta\phi_{\gamma}^{\text{min}} > 0.5$ was found to be an effective discriminant between signal and background for larger bino mass, while the limited kinetic energy available to the bino decay products prohibited the
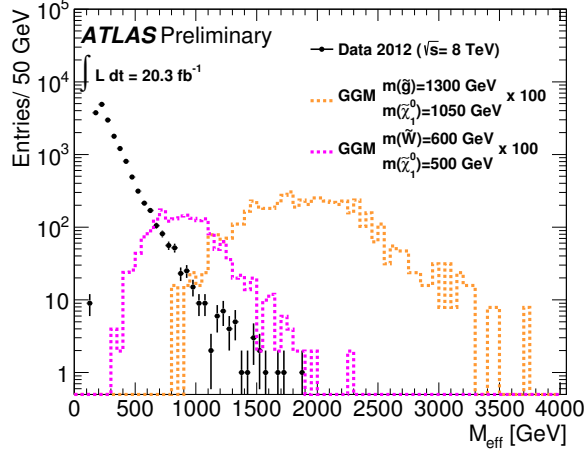
Figure 3: The M_{eff} spectrum of $\gamma\gamma$ candidate events in the data (points, statistical uncertainty only) together with the M_{eff} spectra obtained from gluino production GGM MC samples for $m_{\tilde{g}} = 1300\,\mathrm{GeV}$ and $m_{\tilde{\chi}_1^0} = 1050\,\mathrm{GeV}$, and wino production GGM MC for $m_{\tilde{W}} = 600\,\mathrm{GeV}$ and $m_{\tilde{\chi}_1^0} = 500\,\mathrm{GeV}$. The signal samples are multiplied by a factor of 100 for visibility.

Table 1: Definition of the five SRs based on the quantities $\Delta\phi_\gamma^{\min}$, $\Delta\phi_{\mathrm{jet}}^{\min}$, M_{eff} (or H_T), and E_T^{miss}.

	SP1	SP2	WP1	WP2	MIS
$\Delta\phi_\gamma^{\min} >$	0.5	0.0	0.5	0.0	0.0
$\Delta\phi_{\mathrm{jet}}^{\min} >$	0.5	0.5	0.5	0.5	0.5
$M_{\mathrm{eff}} > (H_T >)$ (GeV)	1500	1800	(400)	(600)	0
$E_T^{\mathrm{miss}} >$ (GeV)	250	150	200	150	250

use of $\Delta\phi_\gamma^{\min}$ as a selection against SM background for lower bino mass. The selection requirements of the five SRs are summarised in Table 1.

Table 2 shows the number of events remaining after several stages of the selection. For the full selection, no events remained for the SP1 and SP2 SRs, while 1, 5 and 2 events remained for the WP1, WP2 and MIS SRs, respectively.

As an example of the results of the selection requirements, Fig. 4 shows the E_T^{miss} distribution for the sample arising from the application of all of the SP1 (WP2) selection criteria save the E_T^{miss} requirement. The expected backgrounds (discussed in Section 6) are overlaid, divided into the three contributing sources. Also shown is the signal expectation for the $(m_{\tilde{g}}, m_{\tilde{\chi}_1^0}) = (1300, 1050)$ $((m_{\tilde{W}}, m_{\tilde{\chi}_1^0}) = (600, 500))$ GeV model, scaled up by x10 (x100) for the sake of visibility.

6 Background estimation

The SM background contributions can be grouped into three primary components. The first of these, referred to as 'QCD background', arises primarily from a mixture of processes that include $\gamma\gamma$ production as well as γ + jet and multijet events with at least one jet mis-reconstructed as a photon. The second background component, referred to as 'EW background', is due primarily to $W + X$ (here 'X' can be any number of jets, accompanied by no more than one photon; the two-photon case is treated separately) and $t\bar{t}$ events, with a smaller contribution arising from $Z + X$ events. These events tend to include final-state

6

Table 2: Numbers of selected data events at progressive stages of the selection. A dash signifies that the cut was not applied.

Selection Stage	SP1	SP2	WP1	WP2	MIS
Triggered Events			10710701		
2 Photons $E_T > 75$ GeV			17458		
$\Delta\phi_{\mathrm{jet}}^{\mathrm{min}} > 0.5$			17005		
$\Delta\phi_{\gamma}^{\mathrm{min}} > 0.5$	11322	–	11322	–	–
M_{eff} or H_T requirement	1	1	1179	485	–
E_T^{miss} requirement	0	0	1	5	2

neutrinos that produce significant E_T^{miss}. In both cases, EW background events entering the signal regions generally have at least one electron mis-reconstructed as a photon. The QCD and EW backgrounds were estimated via dedicated control samples of data events.

The third background component, referred to as 'irreducible', consists of W and Z bosons produced in association with two real photons, with a subsequent decay into one or more neutrinos. Of this background, the $W(\to \ell\nu) + \gamma\gamma$ component dominates, and requires corrections to its LO contribution that are both large and rapidly-varying across the phase space of the $W(\to \ell\nu) + \gamma\gamma$ (plus possible additional jets) phase space [51]. Thus a new, data-driven approach has been developed to constrain the $W(\to \ell\nu) + \gamma\gamma$ contribution to the five SRs. As for prior analyses, the $Z(\to \nu\bar{\nu}) + \gamma\gamma$ contribution is estimated directly from MC.

To estimate the QCD background in the five SRs, a 'QCD control sample' was selected from the diphoton trigger sample by selecting events for which one photon candidate passes the tight selection criteria, while the other passes the loose but not the tight photon criteria. Studies with MC simulated samples as well as E_T^{miss} and H_T sideband data suggest that the E_T^{miss} distribution of this control sample reproduces the E_T^{miss} distribution of the QCD background in the high-E_T^{miss} region used for the signal selection. Electrons were vetoed to reduce contamination from $W \to e\nu$ decays. The H_T, M_{eff}, $\Delta\phi_{\mathrm{jet}}^{\mathrm{min}}$ and $\Delta\phi_{\gamma}^{\mathrm{min}}$ requirements associated with each of the five SRs were then applied, yielding five separate QCD control samples from which E_T^{miss}-distribution 'templates' were derived. An estimate of the QCD background contamination in each SR was obtained by imposing the E_T^{miss} requirement associated with the given SR upon the corresponding QCD template, after normalising each template to the diphoton data with $E_T^{\mathrm{miss}} < 60$ GeV from the given SR. This yielded 'direct' QCD background expectations of 0.29 ± 0.21(stat), 0.89 ± 0.36(stat), and 0.73 ± 0.28(stat), events for SRs WP1, WP2 and MIS, respectively. Very few events above the corresponding E_T^{miss} requirement were observed for the SP1 and SP2 control samples, yielding poor statistical estimates of the QCD background for those SRs.

To improve the constraint on the estimated background for SRs SP1 and SP2, a complementary method making use of M_{eff} sidebands of the QCD control sample was employed. The M_{eff} requirement applied to the SP1 and SP2 QCD templates was relaxed in 300 GeV steps from the nominal cut value down to zero. For each SR, the E_T^{miss} distribution of each of these extended control samples was scaled to the diphoton E_T^{miss} distribution for $E_T^{\mathrm{miss}} < 60$ GeV of the given SR (making use of the same M_{eff} requirement), yielding a series of expected values for the QCD background as a function of the applied M_{eff} requirement. The complementary estimate for the signal-region background contamination proceeded by employing an extrapolation to the actual M_{eff} requirement used for the analysis (1500 and 1800 GeV for SRs SP1 and SP2, respectively), yielding an expectation of 0.00 and 0.22 events for SRs SP1 and SP2, respectively. Interpreting the asymmetric 68% Poisson range of the direct SP1 and SP2 QCD-background estimates as the uncertainty on the expected QCD background results in estimates of $0.00^{+0.20}_{-0.00}$ and $0.22^{+0.53}_{-0.22}$ events for the SP1 and SP2 SR QCD backgrounds, respectively.

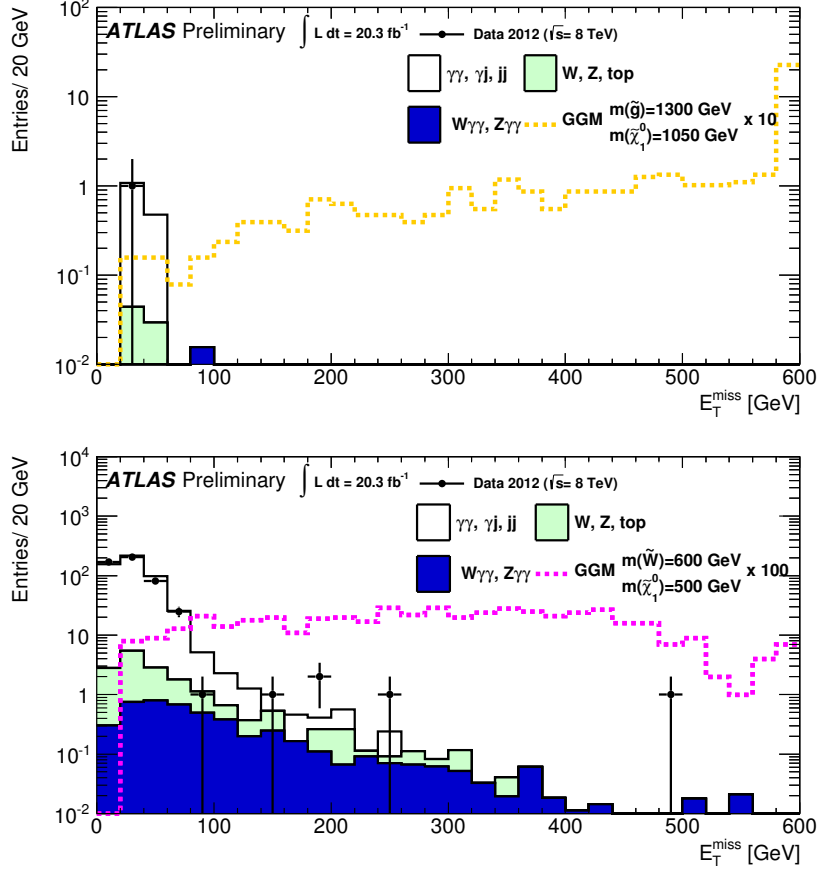Other sources of systematic uncertainty of the estimated QCD background were considered for the

Figure 4: E_T^{miss} spectrum in the SP1 (upper) and WP2 (lower) SRs for the $\gamma\gamma$ candidate events in data (points, statistical uncertainty only) and the estimated QCD background (normalised to the number of $\gamma\gamma$ candidates with $E_T^{miss} < 20$ GeV), the $W(\to e\nu)$ + jets/γ and $t\bar{t}(\to e\nu)$ + jets/γ backgrounds as estimated from the electron-photon control sample, and the irreducible background of $Z(\to \nu\bar{\nu}) + \gamma\gamma$ and $W(\to \ell\nu) + \gamma\gamma$. Also shown are the signal expectations for the $(m_{\tilde{g}}, m_{\tilde{\chi}_1^0}) = (1300, 1050)$ GeV (upper) and $(m_{\tilde{W}}, m_{\tilde{\chi}_1^0}) = (600, 500)$ GeV (lower) models scaled up by x10 and x100, respectively. In both cases the highest E_T^{miss} bin includes events with $E_T^{miss} > 600$ GeV.

WP1, WP2 and MIS SRs. A difference in the $\Delta\phi_{jet}^{min}$ distribution between the QCD control and diphoton samples motivated the assignment of a ±50% uncertainty on the size of the QCD background. Making use of the alternative ranges $20 < E_T^{miss} < 80$ GeV and $40 < E_T^{miss} < 100$ for the normalization of the QCD sample to the $\gamma\gamma$ sample resulted in a further systematic uncertainty of ±45%, ±30% and ±35% on the WP1, WP2, and MIS QCD backgrounds, respectively. The resulting QCD background estimates for the five SRs, along with their uncertainties, are compiled in Table 3.

The EW background (arising primarily from $W + X$ and $t\bar{t}$ events, with a smaller contribution from $Z + X$ events) was estimated via an electron-photon ($e\gamma$) control sample composed of events with at least one tight photon and one electron, each with $E_T > 50$ GeV. This sample was scaled by the probability for an electron to be mis-reconstructed as a tight photon, estimated from the relative rates of $e\gamma$ and ee reconstruction of the $Z \to ee$ sample. To preserve its orthogonality to the signal sample, events with two or more tight photons were vetoed from the control sample. If more than one electron was identified, the one with the highest p_T was used. Because the mis-reconstruction rate depends on the amount of

material in front of the calorimeter, the electron-faking-photon scaling factor was estimated in five bins of $|\eta|$. It varied between 1.9 % ($0 < \eta < 0.6$) and 3.8 % ($-2.47 < \eta < -1.52$).

After applying corresponding selection requirements on H_T, M_{eff}, $\Delta\phi_{\text{jet}}^{\min}$, $\Delta\phi_{\gamma}^{\min}$ and E_T^{miss}, a total of 0 (1) electron-photon events were observed for the SP1 (SP2) SR, 7 (27) electron-photon events were observed for the WP1 (WP2) SR, and 11 electron-photon events were observed for the MIS SR. After multiplying by the η-dependent scaling factor, the resulting EW background contamination was estimated to be < 0.02 (0.02 ± 0.02) events for the SP1 (SP2) SR, 0.15 ± 0.06 (0.67 ± 0.13) events for the WP1 (WP2) SR, and 0.24 ± 0.07 events for the MIS SR, where the uncertainties are statistical only.

MC studies suggest that approximately 25% of the EW background involves no electron-to-photon mis-reconstruction, and thus is not accounted for with the electron-photon control sample. These events, however, typically involve a jet-to-photon mis-reconstruction, and are thus potentially accounted for in the QCD background estimate. A conservative relative systematic uncertainty of $\pm 25\%$ is assigned to the EW background estimates for all five SRs to account for this ambiguity. Including a $\pm 10\%$ uncertainty on the measurement of the electron-to-photon misidentification rate, the resulting EW background estimates for the five SRs are compiled in Table 3.

To estimate the contribution from the irreducible $W(\to \ell\nu) + \gamma\gamma$ process, a control sample of $\gamma\gamma\ell$ events was selected, where ℓ was either an electron or muon with $p_T > 25$ GeV. According to Ref. [51], the LO cross-section for this process is suppressed by a radiation zero, making the K-factor relating the LO cross-section to the full-order process larger than usual. The magnitude of the K-factor is related to the transverse energy of jets that arise from higher-order processes, and, in turn, the recoil scale $p_T^{\ell\gamma\gamma}$ of the diphoton-lepton system. The K-factor is expected to rise significantly for $p_T^{\ell\gamma\gamma} > 100$ GeV, which MC studies suggest is the region that provides the dominant contribution to the $W(\to \ell\nu) + \gamma\gamma$ background after the various SR selections. To this end, events in the $\gamma\gamma\ell$ control sample were also required to have $p_T^{\ell\gamma\gamma} > 100$ GeV. Finally, to further eliminate non-$W(\to \ell\nu) + \gamma\gamma$ backgrounds, but also avoid overlap with the MIS SR, $\gamma\gamma\ell$ events were required to have $50 < E_T^{\text{miss}} < 250$ GeV. The resulting $\gamma\gamma\ell$ sample contained eight events, of which 1.0 ± 0.5 were expected to arise from SM processes other than $W(\to \ell\nu) + \gamma\gamma$. Over much of the gluino-bino and wino-bino parameter space explored in this study, the signal contribution to the $\gamma\gamma\ell$ sample would be quite small; however, for low bino mass the wino-bino model can produce significant signal contamination in the $\gamma\gamma\ell$ control sample. The potential reduction in the measured size of the $W(\to \ell\nu) + \gamma\gamma$ contribution due to the presence of GGM signal in the $\gamma\gamma\ell$ control sample is taken into account when limits are set on the wino mass.

Under the assumption that the signal contribution is zero, the high-$p_T^{\ell\gamma\gamma}$ portion of the $W(\to \ell\nu) + \gamma\gamma$ cross-section can be scaled to produce the observed number of events in the $\gamma\gamma\ell$ control sample, and a corresponding background contribution to the five SRs can be derived using the scaled MC simulation. Contributions arising from the $W(\to \ell\nu) + \gamma\gamma$ process were estimated to be 0.03 ± 0.02 (0.02 ± 0.01) events for the SP1 (SP2) selection, 0.44 ± 0.18 (0.74 ± 0.27) events for the WP1 (WP2) selection, and 0.47 ± 0.19 events for the MIS selection. The uncertainty on these estimates includes statistical uncertainties as well as systematic uncertainties arising from possible variations in the $W(\to \ell\nu) + \gamma\gamma$ K-factor resulting from differences between the control-sample and SR distributions of $p_T^{\ell\gamma\gamma}$.

The contribution of the irreducible background from the $Z(\to \nu\bar{\nu}) + \gamma\gamma$ process was estimated using MC samples, scaled to the LO MadGraph [42] cross-section times a K-factor of 2.0 ± 0.3 [43]. The $Z(\to \nu\bar{\nu}) + \gamma\gamma$ contribution was found to be negligible for SRs SP1 and SP2, and estimated to be 0.13 ± 0.07, 0.08 ± 0.04, and 0.15 ± 0.08 events for SRs WP1, WP2 and MIS, where the uncertainty arises from a 50% scale-factor uncertainty [43] on the K-factor and MC statistics. These estimates, along with the resulting combined estimates for the background from all sources, are reported in Table 3.

9

Table 3: The expected number of observed $\gamma\gamma$ events for each of the five analyses, and the total estimated background, under the assumption that the SUSY signal contribution to the $W(\to \ell\nu) + \gamma\gamma$ control sample is negligible.

Background	SP1	SP2	WP1	WP2	MIS
QCD	$0.00^{+0.20}_{-0.00}$	$0.22^{+0.53}_{-0.22}$	0.29 ± 0.29	0.89 ± 0.60	0.73 ± 0.53
Electroweak	< 0.02	0.02 ± 0.02	0.15 ± 0.07	0.67 ± 0.22	0.24 ± 0.10
$W(\to \ell\nu) + \gamma\gamma$	0.03 ± 0.02	0.02 ± 0.01	0.44 ± 0.18	0.74 ± 0.27	0.47 ± 0.19
$Z(\to \nu\bar{\nu}) + \gamma\gamma$	< 0.01	< 0.01	0.13 ± 0.07	0.08 ± 0.04	0.15 ± 0.08
Total	$0.03^{+0.20}_{-0.02}$	$0.26^{+0.53}_{-0.22}$	1.01 ± 0.36	2.38 ± 0.69	1.59 ± 0.58
Observed events	0	0	1	5	2

7 Signal efficiencies and systematic uncertainties

GGM signal efficiencies were estimated using MC simulation for each simulated point in the $m_{\tilde{g}}, m_{\tilde{\chi}_1^0}$ and $m_{\tilde{W}}, m_{\tilde{\chi}_1^0}$ parameter spaces. For the SP1 analysis the acceptance-times-efficiency of the selection requirements varies from 1.0 % to 16 % across the strong-production grid, increasing smoothly from low values to high values of the gluino and bino masses. For the SP2 analysis the acceptance-times-efficiency of the selection requirements varies from 5.1 % to 15 % across the strong-production grid, with the highest values associated with the highest values of gluino mass, with only small variations observed as a function of bino mass. For the WP1 analysis the acceptance-times-efficiency varies from 1.4 % to 17 % across the weak-production grid, increasing smoothly from low values to high values of the wino and bino masses. For the WP2 analysis the acceptance-times-efficiency varies from 4.1 % to 16 % across the weak-production grid; the highest values are associated with the highest values of wino mass, with only small variations observed as a function of bino mass.

The various relative systematic uncertainties on the signal acceptance-times-efficiency and integrated luminosity are summarised in Table 4, which provides systematic uncertainty ranges for the parameter-space points for which the SP1, SP2, WP1, and WP2 analyses were optimized. The uncertainty on the signal acceptance-times-efficiency is generally dominated by the uncertainty in the calibration of the jet and photon energy scales.

For the 2012 data set the preliminary luminosity uncertainty is 2.8%, based on the calibration procedure described in [50] and using the most recent van der Meer scans performed in November 2012. Making use of a bootstrap method [52], the efficiency of the diphoton trigger was determined to be greater than 99%. The uncertainty on the efficiency of the photon selection, including the isolation requirement, is ±1.5% per photon for both converted and unconverted photons, except for forward ($|\eta_\gamma| > 1.81$) converted photons, for which the efficiency uncertainty is ±2.5%. In portions of the GGM parameter space, uncertainties that varied across the parameter space dominated the systematic uncertainty on the signal acceptance-times-efficiency. The uncertainty on the efficiency due to uncertainties in the photon energy scale is as large as ±11% for the strong-production model and ±17% for electroweak production, with the largest effect appearing at low bino mass in both cases. The uncertainty on the efficiency due to uncertainties in the jet energy scale is as large as ±20% for the strong-production model and ±22% for electroweak production, with the largest effect again appearing at low bino mass. The 'pileup' uncertainty arising from the modeling of additional interactions in the same beam crossing is estimated by varying the distribution of the number of interactions per bunch crossing overlaid in the simulation by ±10%, leading to an uncertainty of less than ±2.2% over the full range of the GGM parameter space. Overall, the quadrature sum of the individual sources of systematic uncertainty on the signal reconstruction

Table 4: Summary of GGM systematic uncertainties in percent. The table has been divided into three sections, enumerating the uncertainties on the integrated luminosity, signal acceptance-times-efficiency, and calculated cross-section, respectively. Although systematic uncertainties are evaluated individually for every simulated signal sample, the uncertainties shown here are for the signal samples used for the optimization of the selection. Specifically, these are the samples generated with $(m_{\tilde{g}}, m_{\tilde{\chi}_1^0}) = (1300, 1050)$ GeV and $(m_{\tilde{g}}, m_{\tilde{\chi}_1^0}) = (1300, 150)$ GeV for SP1 and SP2, respectively, and with $(m_{\tilde{W}}, m_{\tilde{\chi}_1^0}) = (600, 500)$ GeV and $(m_{\tilde{W}}, m_{\tilde{\chi}_1^0}) = (600, 100)$ GeV for WP1 and WP2, respectively.

	Systematic uncertainty			
Selection	SP1	SP2	WP1	WP2
$m_{\tilde{g}}$ ($m_{\tilde{W}}$) (GeV)	1300		(600)	
$m_{\tilde{\chi}_1^0}$ (GeV)	1050	150	500	100
Luminosity	±2.8 %			
Trigger	$(+0.3, -0.4)$ %			
Photon ID (unconverted)	±1.5 %			
Photon ID (converted)	±1.5 % (±2.5 % for $|\eta_\gamma| > 1.81$)			
Photon isolation	Included in Photon ID systematic			
Photon energy scale	±1.6 %	±7.8 %	±5.3 %	±2.3 %
Photon energy resolution	±1.4 %	±0.9 %	±1.9 %	±1.3 %
Jet energy scale	±2.9 %	±14.2 %	±2.2 %	±8.1 %
Jet energy resolution	±1.2 %	±1.8 %	±1.4 %	±0.7 %
Un-reconstructed deposits	< 0.1%	< 0.1%	±0.3 %	±1.5 %
Pileup	±0.1 %	±0.7 %	±0.2 %	±1.2 %
MC statistics	±4.5 %	±4.0 %	±4.2 %	±4.7 %
Total Experimental	±6.9 %	±17.2 %	±8.3 %	±10.6 %
PDF	±32.3 %		±8.4 %	
Scale Uncertainty	±23.0 %		±2.8 %	
Total Theoretical	±35.5 %		±8.6 %	

efficiency ranges between ±2.5% and ±22% over the strong-production parameter space, and between ±4.1% and ±28% over the electroweak-production parameter space, with the largest values arising at lower bino mass.

The PDF and factorisation and renormalisation scale uncertainties on the GGM cross-sections were evaluated as described in Section 2, leading to a combined systematic uncertainty between 23% and 47% for the strong-production GGM model. For the electroweak-production model, the uncertainties were somewhat dependent upon the specific production process ($\tilde{\chi}_2^0 \tilde{\chi}_1^+$, $\tilde{\chi}_2^0 \tilde{\chi}_1^-$ $\tilde{\chi}_1^+ \tilde{\chi}_1^-$), but are less than 13% in all cases, and less than 10% for the combination of all three modes. For the strong-production model, these theoretical uncertainties generate the largest systematic effect on the value of the gluino mass limit arising from the lack of observed events in the SP1 and SP2 signal regions.

8 Results

Table 3 shows the observed numbers of events, along with the size of the expected SM background, in each SR. No evidence for physics beyond the SM was observed in any of the SRs. The largest excess relative to expected background was observed for the WP2 analysis; considering both statistical and systematic uncertainty, and under the assumption that all observed events are from SM sources, an observation of five or more events over an expected background of 2.38 ± 0.69 represents an upward fluctuation with a probability of occurrence of approximately 13%.

Based on the numbers of observed events in the five SRs and the background expectation shown in Table 3, 95 % CL upper limits are set on the number of events in the different SRs from any scenario of physics beyond the SM using the profile likelihood and CL_s prescriptions [53]. Uncertainties on the background expectations are treated as Gaussian-distributed nuisance parameters in the maximum likelihood fit. The upper limit observed for the SP1 (SP2) SR is 3.0 (2.9) events, for the WP1 (WP2) SR is 3.8 (8.3) events, and for the MIS SR 4.7 events. Taking into account the integrated luminosity of (20.3 ± 0.6) fb^{-1} these limits translate into 95 % CL upper limits on the visible cross-section for new physics, defined by the product of cross-section, branching fraction, acceptance and efficiency for the different SR definitions, of 0.15 (0.14) fb for the SP1 (SP2) SR, 0.19 (0.41) fb for the WP1 (WP2) SR, and 0.23 fb for the MIS SR.

By considering, in addition, the value and uncertainty of the acceptance-times-efficiency of the selection requirements associated with the various SRs, as well as the NLO (+NLL) GGM cross-sections [28–32], which vary steeply with gluino (wino) mass for the strong (electroweak) production model, lower limits may be set on the masses of the gluino and wino in the context of these two GGM scenarios. The strong-production SR providing the best expected gluino mass sensitivity is chosen for each simulated model point, leading to a bino-mass transition point of 500 GeV, below which the SP2 analysis is used to establish the limit and above which the SP1 analysis is used. A study of the expected wino mass sensitivity led to the selection of a transition point of 250 GeV for the WP2 and WP1 analyses.

The resulting observed limits are exhibited, as a function of bino mass, for the gluino production and wino production models in Figs. 5 and 6, respectively. For the low bino mass region of the wino-bino parameter space, for which signal contamination in the $W(\to \ell\nu) + \gamma\gamma$ control sample is appreciable, both the normalizaton of the $W(\to \ell\nu) + \gamma\gamma$ background estimate and the limit on the possible number of events from new physics are extracted from a simultaneous fit to the SR and $W(\to \ell\nu) + \gamma\gamma$ control region. Also shown are the expected limits, including their ±1 and ±2 standard-deviation experimental uncertainty ranges, as well as observed limits for SUSY model cross-sections ±1 standard deviation of theoretical uncertainty from their central value. Conservatively choosing the −1 standard deviation contour, a 95% CL lower limit of 1280 GeV (570 GeV) is set on the value of the gluino (wino) mass, for any value of the bino mass above 50 GeV but less than that of the gluino (wino) mass, in the context of this GGM scenario.
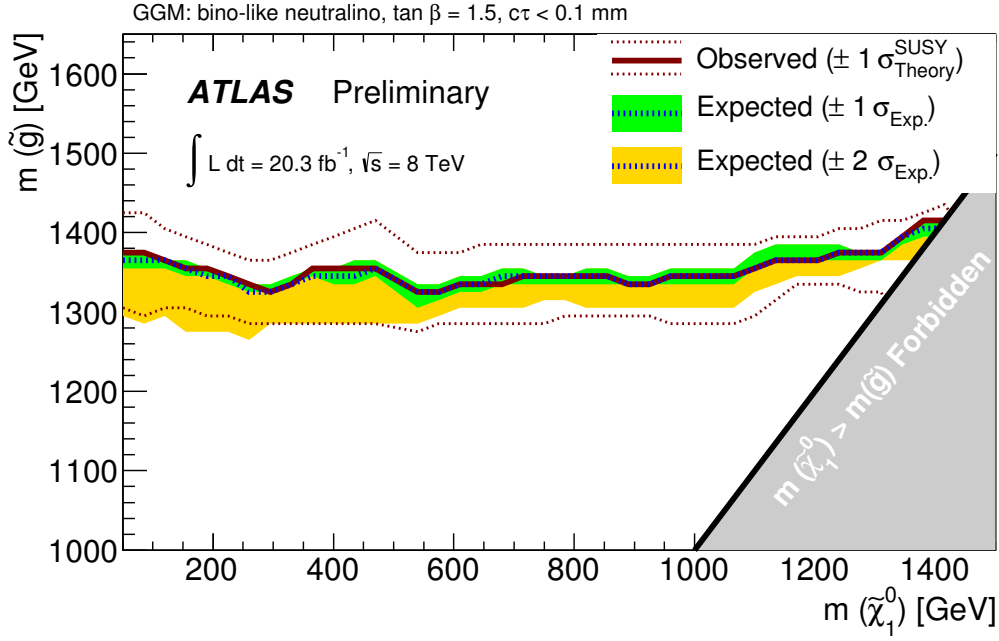
Figure 5: Expected and observed 95 % CL lower limits on the gluino mass as a function of the neutralino mass in the GGM model with a bino-like lightest neutralino NLSP (the grey area indicates the region where the NLSP is the gluino, which is not considered here). The other sparticle masses are decoupled. Further model parameters are $\tan\beta = 1.5$ and $c\tau_{\text{NLSP}} < 0.1\,\text{mm}$. The ± 1 (green) and ± 2 (yellow) standard-deviation expected-limit bands are also displayed. Three observed-limit contours are shown: one for the nominal gluino production cross-section, and one each for a cross-section augmented or diminished by one standard deviation of the cross-section uncertainty. Limits are constrained by the SP2 analysis for $m_{\tilde{\chi}_1^0} < 500\,\text{GeV}$ and by the SP1 analysis for $m_{\tilde{\chi}_1^0} > 500\,\text{GeV}$.

9   Conclusions

A search for events with two photons and substantial $E_{\text{T}}^{\text{miss}}$, performed using 20.3 fb^{-1} of 8 TeV pp collision data recorded with the ATLAS detector at the LHC, has been presented. Inspired by Supersymmetric models incorporating gauge mediation, as well as a model-independent scenario considering only estimated backgrounds, the sensitivity to new physics producing this final state was optimised by defining five different SRs. No significant excess above the expected background is found in any SR. The results are used to set model-independent and model-dependent 95 % CL upper limits on possible contributions from new physics. For a model-independent selection making use of a requirement of $E_{\text{T}}^{\text{miss}} > 250$ GeV to suppress expected backgrounds, an upper limit of 0.23 fb is set on the contribution of new physics to the visible cross-section. Under the GGM hypothesis, lower limits on the gluino and wino masses of 1280 GeV and 570 GeV, respectively, are determined for bino masses above 50 GeV.

References

[1] H. Miyazawa, *Baryon Number Changing Currents*, Prog. Theor. Phys. **36 (6)** (1966) 1266.

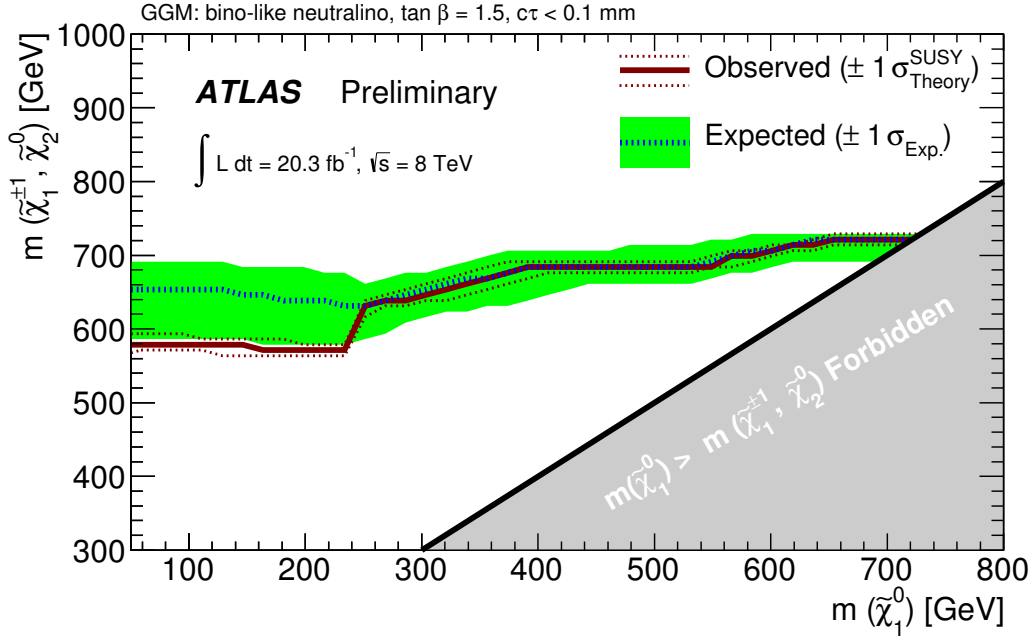[2] P. Ramond, *Dual Theory for Free Fermions*, Phys. Rev. **D3** (1971) 2415.

Figure 6: Expected and observed 95 % CL lower limits on the wino mass as a function of the neutralino mass in the GGM model with a bino-like lightest neutralino NLSP (the grey area indicates the region where the NLSP is the wino, which is not considered here). The other sparticle masses are decoupled. Further model parameters are $\tan\beta = 1.5$ and $c\tau_{\text{NLSP}} < 0.1$ mm. The ± 1 standard-deviation expected-limit band (green) is also displayed. Three observed-limit contours are shown: one for the nominal wino production cross-section, and one each for a cross-section augmented or diminished by one standard deviation of the cross-section uncertainty. Limits are constrained by the WP2 analysis for $m_{\tilde{\chi}_1^0} < 250$ GeV and by the WP1 analysis for $m_{\tilde{\chi}_1^0} > 250$ GeV.

[3] Y. A. Gol'fand and E. P. Likhtman, *Extension of the Algebra of Poincare Group Generators and Violation of p Invariance*, JETP Lett. **13** (1971) 323. [Pisma Zh.Eksp.Teor.Fiz.13:452-455,1971].

[4] A. Neveu and J. H. Schwarz, *Factorizable Dual Model of Pions*, Nucl. Phys. **B31** (1971) 86.

[5] A. Neveu and J. H. Schwarz, *Quark Model of Dual Pions*, Phys. Rev. **D4** (1971) 1109.

[6] J. Gervais and B. Sakita, *Field Theory Interpretation of Supergauges in Dual Models*, Nucl. Phys. **B34** (1971) 632.

[7] D. V. Volkov and V. P. Akulov, *Is the Neutrino a Goldstone Particle?*, Phys. Lett. **B46** (1973) 109.

[8] J. Wess and B. Zumino, *A Lagrangian Model Invariant Under Supergauge Transformations*, Phys. Lett. **B49** (1974) 52.

[9] J. Wess and B. Zumino, *Supergauge Transformations in Four-Dimensions*, Nucl. Phys. **B70** (1974) 39.

[10] P. Fayet, *Supersymmetry and Weak, Electromagnetic and Strong Interactions*, Phys. Lett. **B64** (1976) 159.

[11] P. Fayet, *Spontaneously Broken Supersymmetric Theories of Weak, Electromagnetic and Strong Interactions*, Phys. Lett. **B69** (1977) 489.

[12] G. R. Farrar and P. Fayet, *Phenomenology of the Production, Decay, and Detection of New Hadronic States Associated with Supersymmetry*, Phys. Lett. **B76** (1978) 575.

[13] P. Fayet, *Relations Between the Masses of the Superpartners of Leptons and Quarks, the Goldstino Couplings and the Neutral Currents*, Phys. Lett. **B84** (1979) 416.

[14] S. Dimopoulos and H. Georgi, *Softly Broken Supersymmetry and SU(5)*, Nucl. Phys. **B193** (1981) 150.

[15] M. Dine and W. Fischler, *A Phenomenological Model of Particle Physics Based on Supersymmetry*, Phys. Lett. **B110** (1982) 227.

[16] L. Alvarez-Gaume, M. Claudson, and M. B. Wise, *Low-Energy Supersymmetry*, Nucl. Phys. **B207** (1982) 96.

[17] C. R. Nappi and B. A. Ovrut, *Supersymmetric Extension of the SU(3) x SU(2) x U(1) Model*, Phys. Lett. **B113** (1982) 175.

[18] M. Dine and A. E. Nelson, *Dynamical Supersymmetry Breaking at Low-energies*, Phys. Rev. **D48** (1993) 1277, `arXiv:hep-ph/9303230`.

[19] M. Dine, A. E. Nelson, and Y. Shirman, *Low-Energy Dynamical Supersymmetry Breaking Simplified*, Phys. Rev. **D51** (1995) 1362, `arXiv:hep-ph/9408384`.

[20] M. Dine, A. E. Nelson, Y. Nir, and Y. Shirman, *New Tools for Low-Energy Dynamical Supersymmetry Breaking*, Phys. Rev. **D53** (1996) 2658, `arXiv:hep-ph/9507378`.

[21] P. Meade, N. Seiberg, and D. Shih, *General Gauge Mediation*, Prog. Theor. Phys. Suppl. **177** (2009) 143, `arXiv:0801.3278 [hep-ph]`.

[22] M. Buican, P. Meade, N. Seiberg, and D. Shih, *Exploring General Gauge Mediation*, JHEP **03** (2009) 016, `arXiv:0812.3668 [hep-ph]`.

[23] ATLAS Collaboration, *Search for diphoton events with large missing transverse momentum in 7 TeV proton-proton collision data with the ATLAS detector*, Phys. Lett. **B718** (2012) 411, `arXiv:1209.0753 [hep-ex]`.

[24] A. Djouadi, J.-L. Kneur, and G. Moultaka, *SuSpect: A Fortran Code for the Supersymmetric and Higgs Particle Spectrum in the MSSM*, Comput. Phys. Commun. **176** (2007) 426, `arXiv:hep-ph/0211331`.

[25] M. Muhlleitner, A. Djouadi, and Y. Mambrini, *SDECAY: A Fortran Code for the Decays of the Supersymmetric Particles in the MSSM*, Comput. Phys. Commun. **168** (2005) 46, `arXiv:hep-ph/0311167`.

[26] M. Bahr et al., *Herwig++ Physics and Manual*, Eur. Phys. J. **C58** (2008) 639, `arXiv:0803.0883 [hep-ph]`.

[27] A. Sherstnev and R. S. Thorne, *Parton Distributions for LO Generators*, Eur. Phys. J. **C55** (2008) 553, `arXiv:0711.2473 [hep-ph]`.

[28] W. Beenakker, R. Hopker, M. Spira, and P. Zerwas, *Squark and Gluino Production at Hadron Colliders*, Nucl. Phys. **B492** (1997) 51, arXiv:hep-ph/9610490.

[29] A. Kulesza and L. Motyka, *Threshold Resummation for Squark-Antisquark and Gluino-pair Production at the LHC*, Phys. Rev. Lett. **102** (2009) 111802, arXiv:0807.2405 [hep-ph].

[30] A. Kulesza and L. Motyka, *Soft Gluon Resummation for the Production of Gluino-Gluino and Squark-Antisquark Pairs at the LHC*, Phys. Rev. **D80** (2009) 095004, arXiv:0905.4749 [hep-ph].

[31] W. Beenakker et al., *Soft-Gluon Resummation for Squark and Gluino Hadroproduction*, JHEP **0912** (2009) 041, arXiv:0909.4418 [hep-ph].

[32] W. Beenakker et al., *Squark and Gluino Hadroproduction*, Int. J. Mod. Phys. **A26** (2011) 2637–2664, arXiv:1105.1110 [hep-ph].

[33] M. Kramer et al., *Supersymmetry Production Cross Sections in pp Collisions at $\sqrt{s} = 7$ TeV*, arXiv:1206.2892 [hep-ph].

[34] M. Mangano et al., *ALPGEN, a generator for hard multiparton processes in hadronic collisions*, JHEP **07** (2003) 001, arXiv:hep-ph/0206293.

[35] J. Butterworth, J. Forshaw, and M. Seymour, *Multiparton interactions in photoproduction at HERA*, Z. Phys. **C72** (1996) 637–646, hep-ph/9601371.

[36] D. Stump et al., *Inclusive Jet Production, Parton Distributions, and the Search for New Physics*, JHEP **10** (2003) 046, arXiv:hep-ph/0303013.

[37] H.-L. Lai et al., *New Parton Distributions For Collider Physics*, Phys. Rev. **D82** (2010) 074024, arXiv:1007.2241 [hep-ph].

[38] T. Gleisberg et al., *Event Generation With SHERPA 1.1*, JHEP **10** (2009) 007, arXiv:0811.4622 [hep-ph].

[39] S. Frixione and B. R. Webber, *The MC@NLO 3.2 event generator*, arXiv:hep-ph/0601192.

[40] S. Frixione and B. R. Webber, *Matching NLO QCD computations and parton shower simulations*, JHEP **06** (2002) 029, arXiv:hep-ph/0204244.

[41] T. Sjostrand, S. Mrenna, and P. Skands, *PYTHIA 6.4 Physics and Manual*, JHEP **05** (2006) 026, arXiv:hep-ph/0603175.

[42] J. Alwall et al., *MadGraph 5: Going Beyond*, JHEP **1106** (2011) 128, arXiv:1106.0522 [hep-ph].

[43] G. Bozzi, F. Campanario, M. Rauch, and D. Zeppenfeld, *Zγγ Production with Leptonic Decays and Triple Photon Production at NLO QCD*, Phys.Rev. **D84** (2011) 074028, arXiv:1107.3149 [hep-ph].

[44] GEANT4 Collaboration, S. Agostinelli et al., *GEANT4: A Simulation Toolkit*, Nucl. Instrum. Meth. **A506** (2003) 250.

[45] ATLAS Collaboration, *The ATLAS Simulation Infrastructure*, Eur. Phys. J. **C70** (2010) 823, arXiv:1005.4568 [physics.ins-det].

[46] ATLAS Collaboration, *The ATLAS Experiment at the CERN Large Hadron Collider*, JINST **3** (2008) S08003.

[47] ATLAS Collaboration, *Measurement of the Inclusive Isolated Prompt Photon Cross Section in pp Collisions at $\sqrt{s}$ = 7 TeV with the ATLAS Detector*, Phys. Rev. **D83** (2011) 052005, `arXiv:1012.4389 [hep-ex]`.

[48] ATLAS Collaboration, *Electron Performance Measurements with the ATLAS Detector Using the 2010 LHC Proton-Proton Collision Data*, Eur. Phys. J. **C72** (2012) 1909, `arXiv:1110.3174 [hep-ex]`.

[49] M. Cacciari, G. Salam, and G. Soyez, *The Anti-k_t Jet Clustering Algorithm*, JHEP **04** (2008) 063, `arXiv:0802.1189`.

[50] ATLAS Collaboration, *Improved luminosity determination in pp collisions at sqrts = 7 TeV using the ATLAS detector at the LHC*, Arxiv:1105.3152.

[51] G. Bozzi, F. Campanario, M. Rauch, and D. Zeppenfeld, *$W\gamma\gamma$ Production with Leptonic Decays at NLO QCD*, Phys. Rev. **D83** (2011) 114035, `arXiv:1103.4613 [hep-ph]`.

[52] ATLAS Collaboration, *Performance of the ATLAS Electron and Photon Trigger in p-p Collisions at sqrts = 7 TeV in 2011*, Tech. Rep. ATLAS-CONF-2012-048, CERN, Geneva, May, 2012.

[53] A. L. Read, *Presentation of Search Results: The CL_s Technique*, J. Phys. **G28** (2002) 2693.

Selection Stage	SP1	SP2	WP1	WP2
$m_{\tilde{g}}$ ($m_{\tilde{W}}$)	1300	1300	600	600
$m_{\tilde{\chi}_1^0}$	1050	150	500	100
All Generated	5000 (39.4)		5000 (99.3)	
Triggered Events	2979 (23.5)	3492 (27.5)	2994 (59.5)	3598 (71.5)
2 Photons $E_T > 75$ GeV	930 (7.3)	1017 (8.0)	980 (19.5)	1072 (21.2)
$\Delta\phi_{\text{jet}}^{\min} > 0.5$	712 (5.6)	879 (6.9)	928 (18.5)	944 (18.8)
$\Delta\phi_{\gamma}^{\min} > 0.5$	665 (5.2)	–	874 (17.4)	–
M_{eff} or H_T requirement	551 (4.3)	779 (6.1)	810 (16.1)	857 (17.0)
E_T^{miss} requirement	499 (3.9)	625 (4.9)	579 (11.5)	457 (9.0)

Table 5: MC cut-flow results for the four model points used to tune the SP1, SP2, WP1, and WP2 selections. Both raw event numbers relative to a generated sample of 5000 events and, in parentheses, expected event numbers scaled to an integrated luminosity of 20.3 fb^{-1} are shown. As shown in the table by way of reminder, the mass parameters of the four points used for tuning are $(m_{\tilde{g}}, m_{\tilde{\chi}_1^0}) = (1300, 1050)$, $(m_{\tilde{g}}, m_{\tilde{\chi}_1^0}) = (1300, 150)$, $(m_{\tilde{W}}, m_{\tilde{\chi}_1^0}) = (600, 500)$, and $(m_{\tilde{W}}, m_{\tilde{\chi}_1^0}) = (600, 100)$, respectively.

A Signal Cut Flow

Event sample numbers after the successive application of the selection cuts are shown for typical MC signal samples in Table 5.

B Expected Sensitivity Studies

In this Appendix we provide further background on the expected gluino and wino mass sensitivity studies mentioned in Section 8. Based on the number of expected background events, ignoring possible signal contamination in the $W(\to \ell\nu) + \gamma\gamma$ control region, and assuming a uniform signal acceptance-times-efficiency uncertainty of ±25%, we have calculated expected lower limits on the gluino (wino) mass as a function of the assumed bino mass for the SP1 and SP2 (WP1 and WP2) analyses. Since our model points are not dense in the free parameter space, no single point is expected to have a test statistic of exactly $p = 0.05$. Instead, we draw a smooth function to the calculated test statistic across the discrete grid and draw our limit at the locus of points at which that function crosses the level $p = 0.05$, providing an expected limit as a function of bino mass in the gluino/bino mass plane for analyses SP1 and SP2, and in the wino/bino mass plane for analyses WP1 and WP2.

These approximate expected limits, representing an estimate of the expected gluino and wino mass sensitivities, are exhibited separately for SP1 and SP2 in Fig. 7. Based on this study, it was decided to use the SP2 analysis for bino masses below 500 GeV and the SP1 analysis for bino masses above that. These approximate expected limits are exhibited separately for WP1 and WP2 in Fig. 8. Based on this study, it was decided to use the WP2 analysis for bino masses below 250 GeV and the WP1 analysis for bino masses above that. For both figures, the analysis yielding the best expected mass limit is shown for each point in the associated GGM grid.

C Production Cross-Section Limits

Figures 9 and 10 are a reproduction of the limit-contour plots of Figs. 5 and 6, but also include the lower bound of the excluded production cross-section (in fb^{-1}), displayed at each grid point.
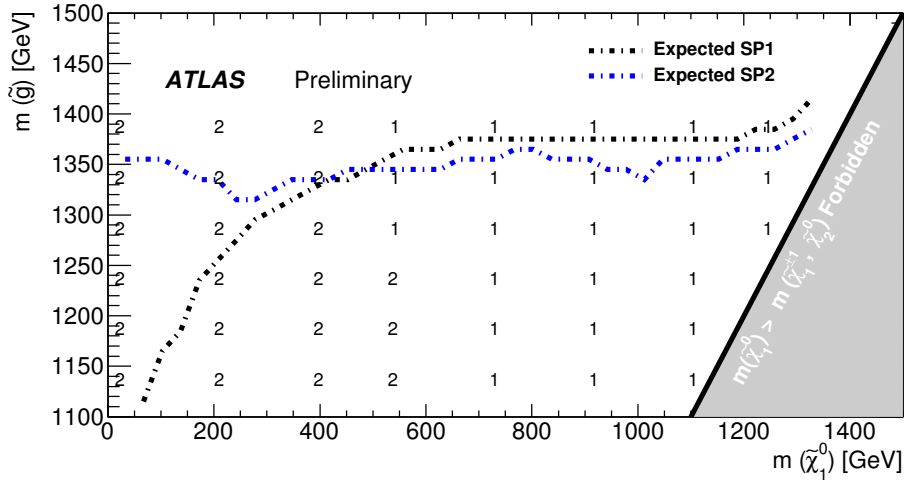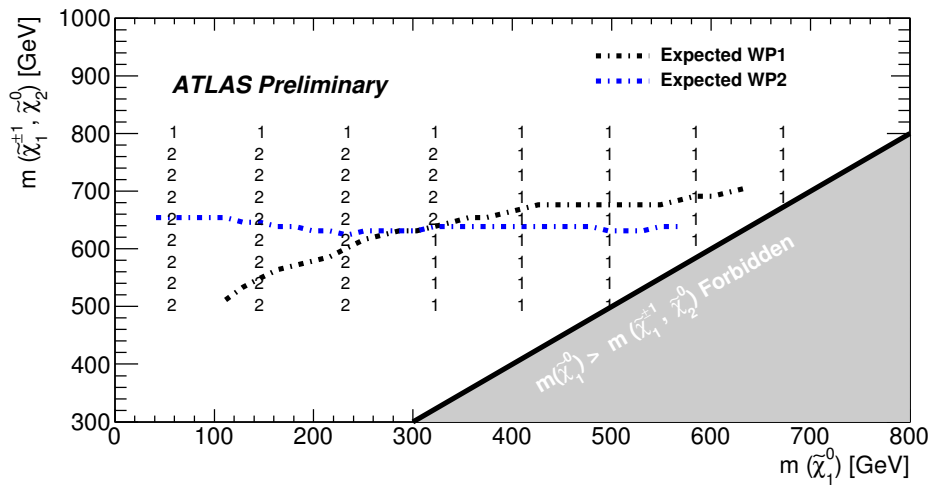
Figure 7: Expected gluino mass sensitivity for the SP1 and SP2 analyses across the gluino/bino phase space. Based on this result, it was decided to use the SP2 analysis for bino masses below 500 GeV and the SP1 analysis for bino masses above that. It is assumed that the number of observed events is that of the expected background of Table 3. A uniform signal acceptance-times-efficiency systematic of ±25% is also assumed. The numeral at each grid point indicates which of the two analyses (SP1 or SP2) provides the best expected mass limit for that point.

D   Event Displays

Event displays for the six selected events. The events selected by the WP2 analysis are shown in Figs. 11, 13, 14, 15 and 16. The events selected by the MIS analysis are shown in Figs. 11 and 12. The event selected by the WP1 analysis is shown in Fig. 13.

Figure 8: Expected wino mass sensitivity for the WP1 and WP2 analyses across the wino/bino phase space. Based on this result, it was decided to use the WP2 analysis for bino masses below 250 GeV and the WP1 analysis for bino masses above that. It is assumed that the number of observed events is that of the expected background of Table 3. A uniform signal acceptance-times-efficiency systematic of ±25% is also assumed. The numeral at each grid point indicates which of the two analyses (WP1 or WP2) provides the best expected mass limit for that point.
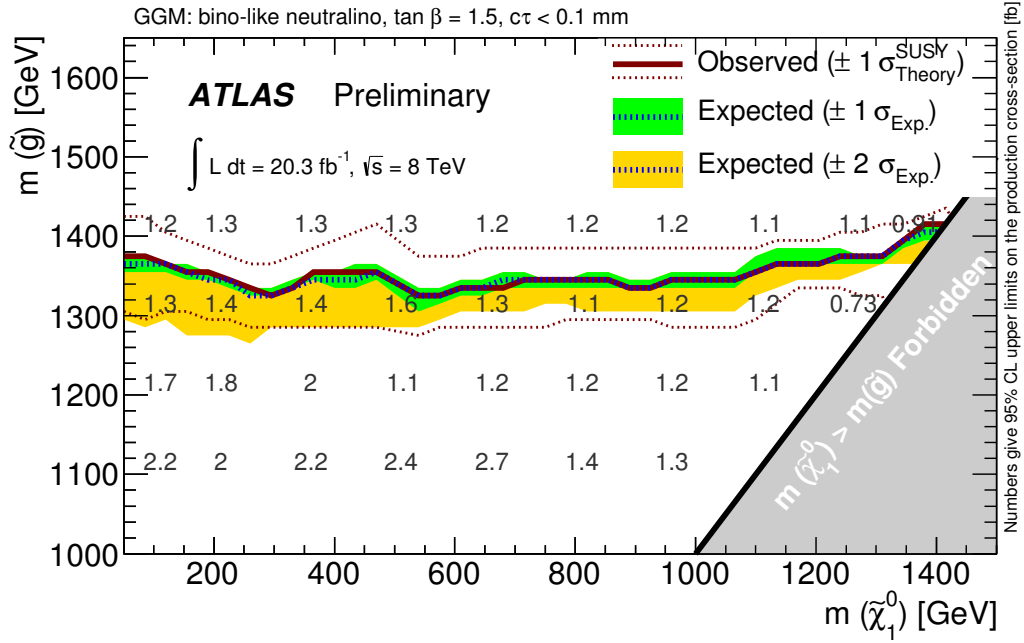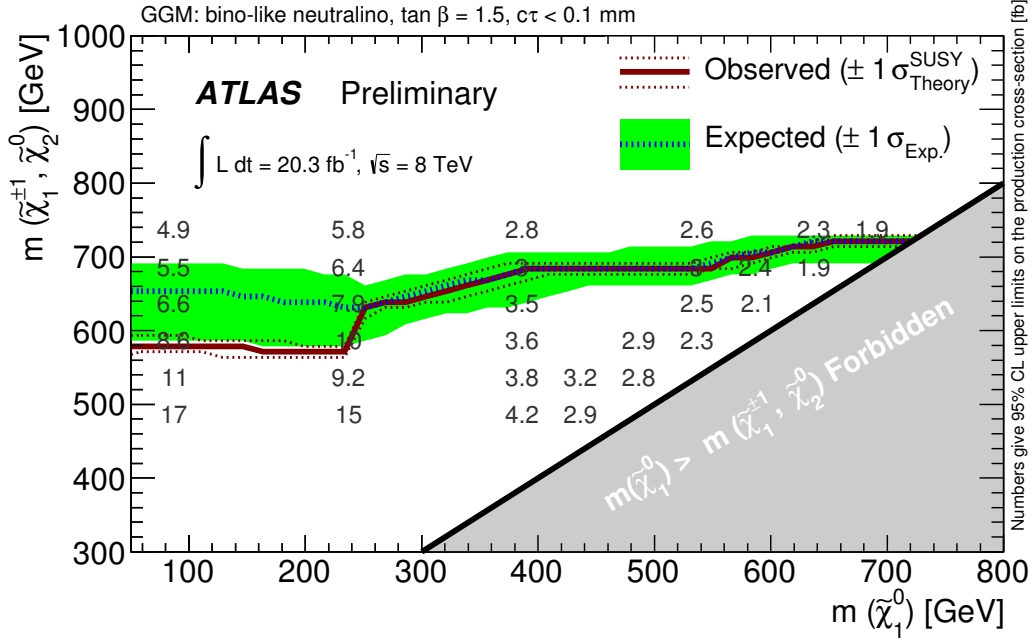
Figure 9: Expected and observed 95 % CL lower limits on the gluino mass as a function of the neutralino mass in the GGM model with a bino-like lightest neutralino NLSP (the grey area indicates the region where the NLSP is the gluino, which is not considered here). The other sparticle masses are decoupled. Further model parameters are $\tan\beta = 1.5$ and $c\tau_{NLSP} < 0.1$ mm. The lower bound of the excluded cross-section (in fb) is displayed at each grid point. The ±1 (green) and ±2 (yellow) standard-deviation expected-limit bands are also displayed. Three observed-limit contours are shown: one for the nominal gluino production cross-section, and one each for a cross-section augmented or diminished by one standard deviation of the cross-section uncertainty. Limits are constrained by the SP2 analysis for $m_{\tilde{\chi}_1^0} < 500$ GeV and by the SP1 analysis for $m_{\tilde{\chi}_1^0} > 500$ GeV.

Figure 10: Expected and observed 95 % CL lower limits on the wino mass as a function of the neutralino mass in the GGM model with a bino-like lightest neutralino NLSP (the grey area indicates the region where the NLSP is the wino, which is not considered here). The other sparticle masses are decoupled. Further model parameters are $\tan\beta = 1.5$ and $c\tau_{\mathrm{NLSP}} < 0.1$ mm. The lower bound of the excluded cross-section (in fb) is displayed at each grid point. The ± 1 standard-deviation expected-limit band (green) is also displayed. Three observed-limit contours are shown: one for the nominal wino production cross-section, and one each for a cross-section augmented or diminished by one standard deviation of the cross-section uncertainty. Limits are constrained by the WP2 analysis for $m_{\tilde{\chi}_1^0} < 250$ GeV and by the WP1 analysis for $m_{\tilde{\chi}_1^0} > 250$ GeV.
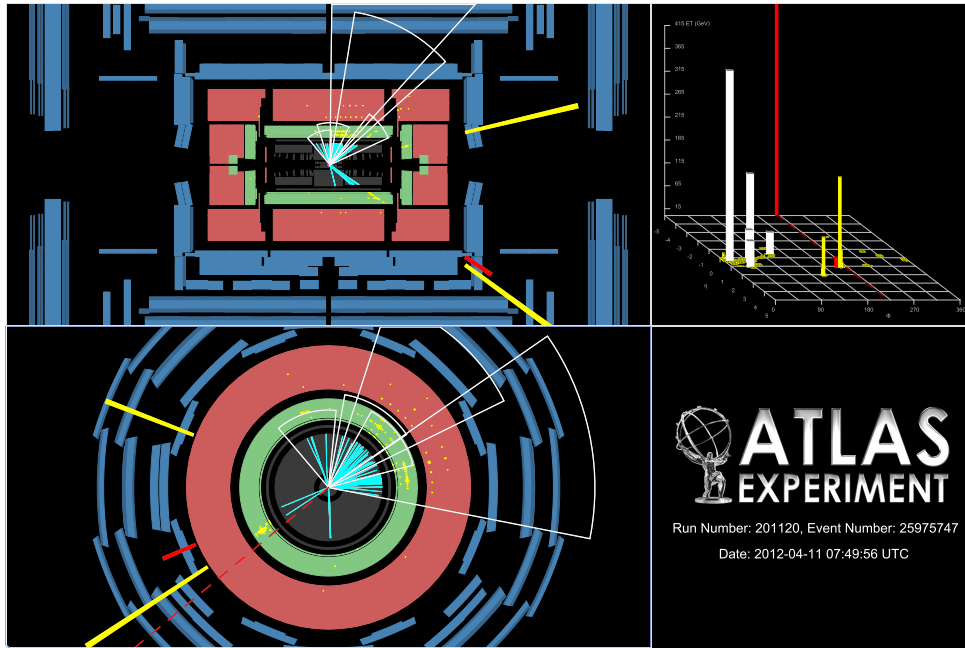
Figure 11: Event display for run 201120 event 25975747. This event was selected by the MIS and WP2 selections. Reconstructed tracks are displayed only if their transverse momentum is greater than 2.5 GeV. The E_T of the two leading photons was measured to be 197 and 84 GeV, while E_T^{miss} was measured to be 478 GeV. The event has five reconstructed jets with $p_T > 30$ GeV.
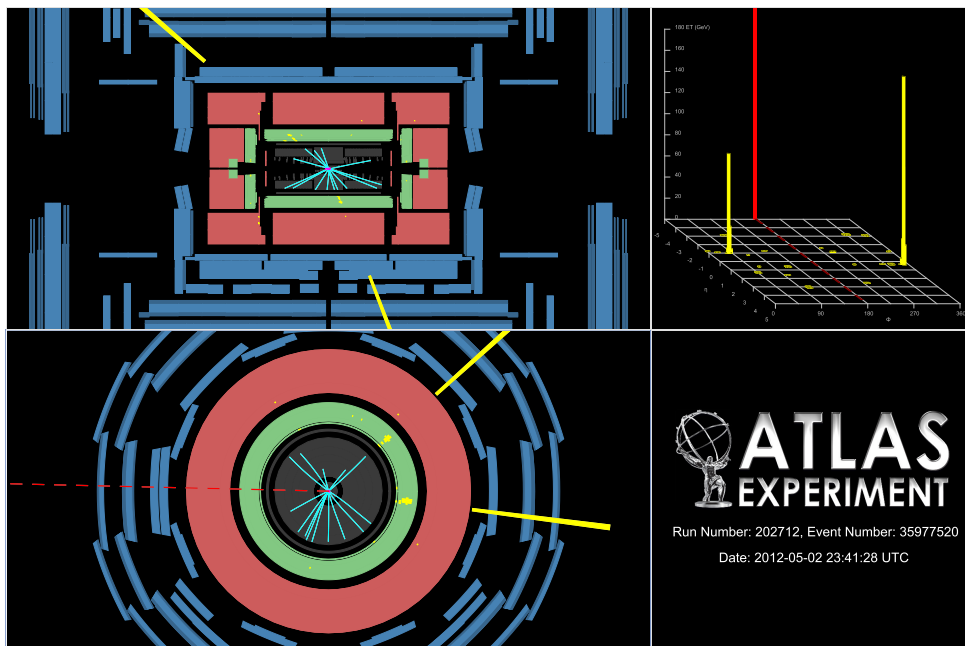

Figure 12: Event display for run 202712 event 35977520. This event was selected by the MIS selection. Reconstructed tracks are displayed only if their transverse momentum is greater than 2.5 GeV. The E_T of the two leading photons was measured to be 178 and 94 GeV, while E_T^{miss} was measured to be 276 GeV. The event has no reconstructed jets with $p_T > 30$ GeV.
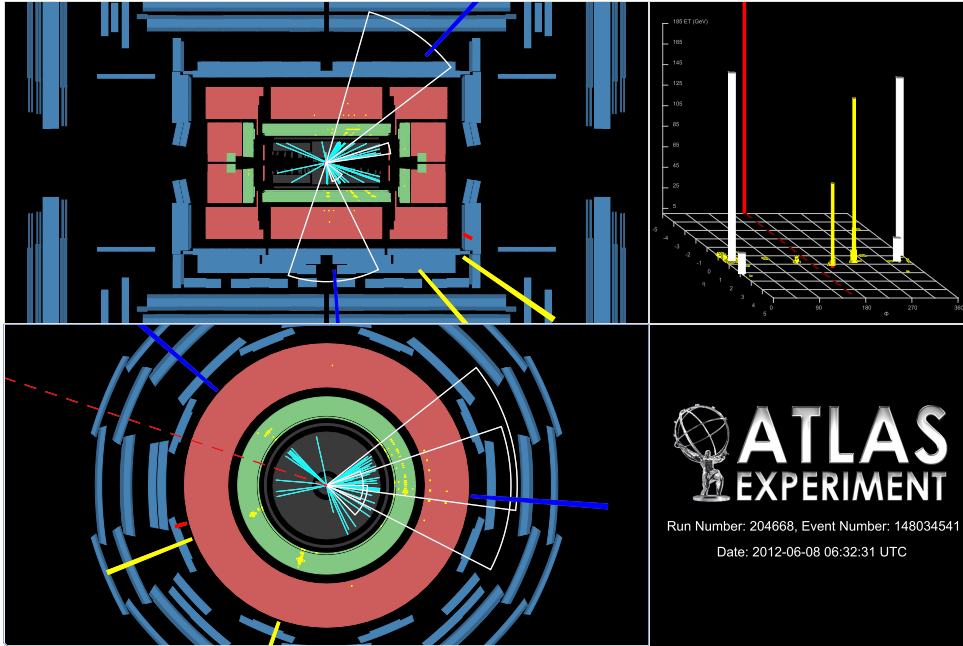
Figure 13: Event display for run 204668 event 148034541. This event was selected by the WP1 and WP2 selections. Reconstructed tracks are displayed only if their transverse momentum is greater than 2.5 GeV. The E_T of the two leading photons was measured to be 159 and 80 GeV, while E_T^{miss} was measured to be 245 GeV. The event has two reconstructed jets with $p_T > 30$ GeV.
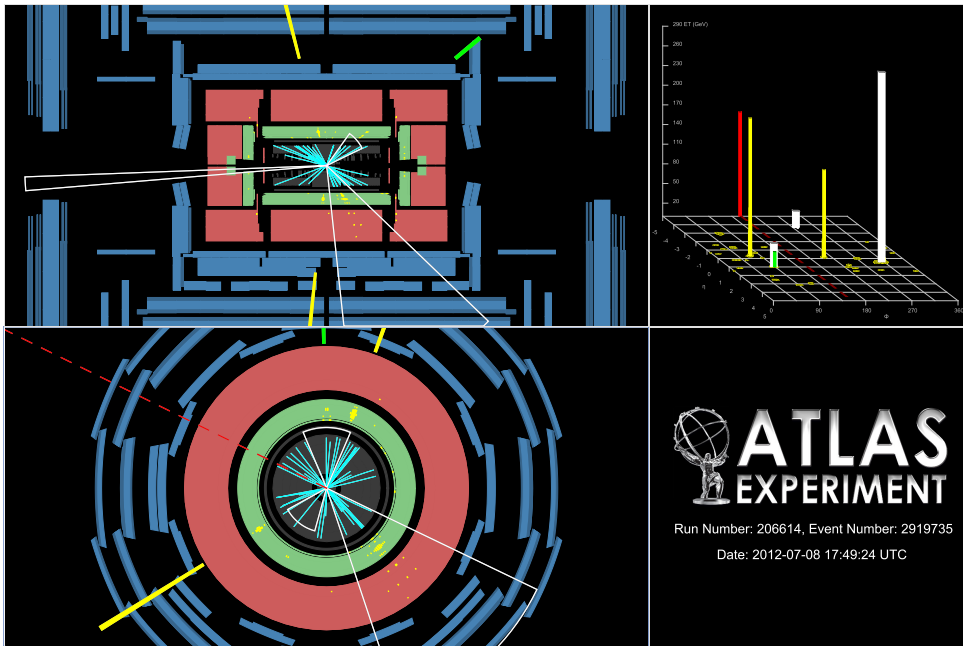

Figure 14: Event display for run 206614 event 2919735. This event was selected by the WP2 selection. Reconstructed tracks are displayed only if their transverse momentum is greater than 2.5 GeV. The E_T of the two leading photons was measured to be 210 and 133 GeV, while E_T^{miss} was measured to be 159 GeV. The event has two reconstructed jets with $p_T > 30$ GeV.
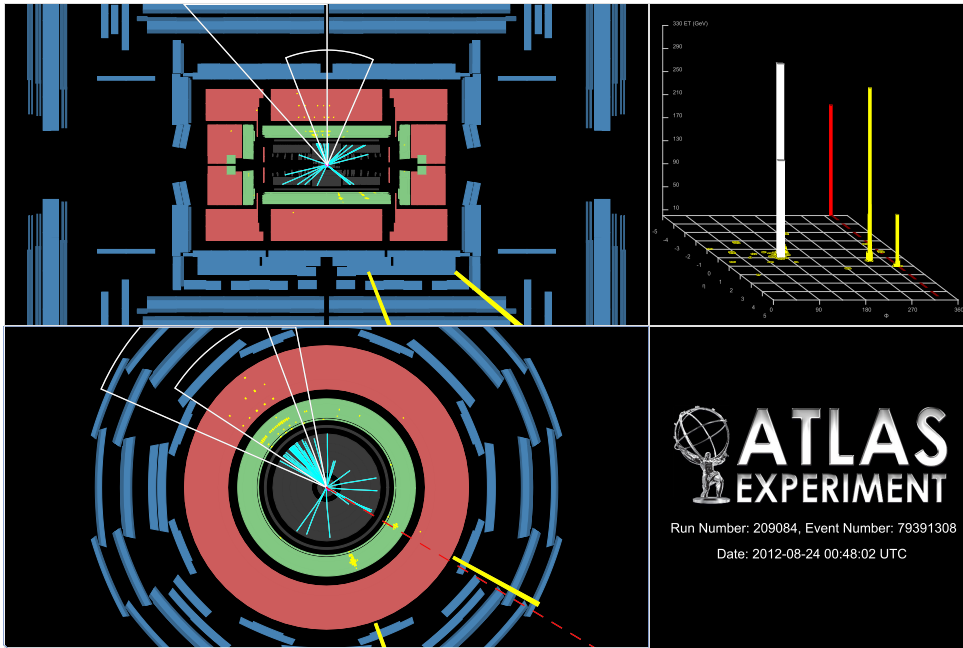
Figure 15: Event display for run 209084 event 79391308. This event was selected by the WP2 selection. Reconstructed tracks are displayed only if their transverse momentum is greater than 2.5 GeV. The E_T of the two leading photons was measured to be 300 and 89 GeV, while E_T^{miss} was measured to be 192 GeV. The event has two reconstructed jets with $p_T > 30$ GeV.
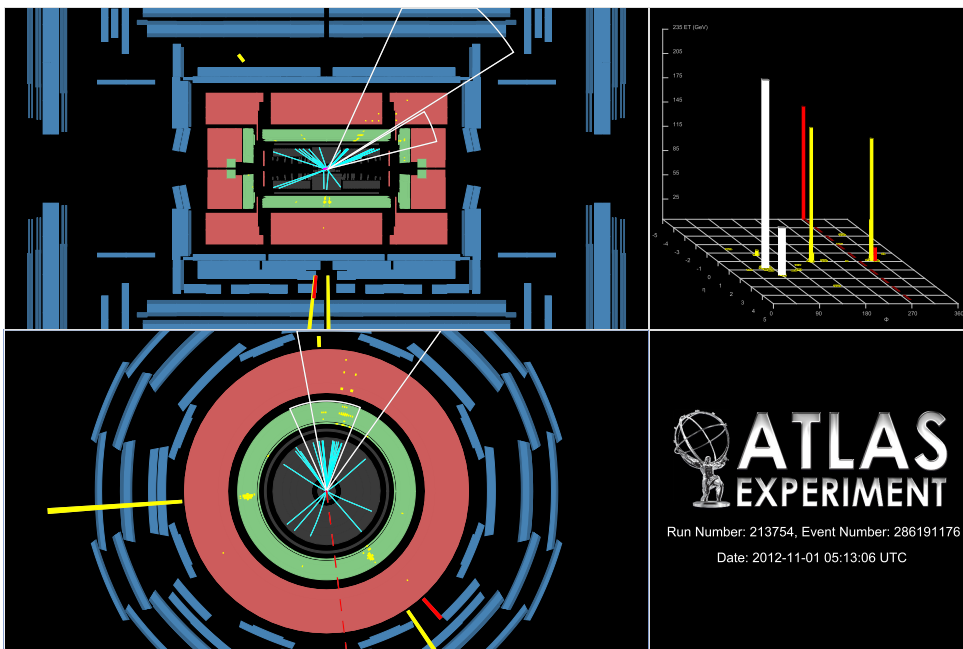

Figure 16: Event display for run 213754 event 286191176. This event was selected by the WP2 selection. Reconstructed tracks are displayed only if their transverse momentum is greater than 2.5 GeV. The E_T of the two leading photons was measured to be 165 and 150 GeV, while E_T^{miss} was measured to be 139 GeV. The event has two reconstructed jets with $p_T > 30$ GeV.